Plasma Physics and Controlled Fusion

PAPER • OPEN ACCESS

Overview over the neutral gas pressures in Wendelstein 7-X during divertor operation under boronized wall conditions

To cite this article: V Haak *et al* 2023 *Plasma Phys. Control. Fusion* **65** 055024

View the article online for updates and enhancements.

You may also like

- Scrape-off layer transport and filament characteristics in high-density tokamak regimes
N. Vianello, D. Carralero, C.K. Tsui et al.

- Impurity transport and divertor retention in Ar and N seeded SOLPS 5.0 simulations for ASDEX Upgrade
F Hitzler, M Wischmeier, F Reimold et al.

- First divertor physics studies in Wendelstein 7-X
T. Sunn Pedersen, R. König, M. Jakubowski et al.

This content was downloaded from IP address 141.52.248.2 on 21/04/2023 at 11:30

OPEN ACCESS
IOP Publishing
Plasma Physics and Controlled Fusion
Plasma Phys. Control. Fusion **65** (2023) 055024 (16pp)
https://doi.org/10.1088/1361-6587/acc8fb

Overview over the neutral gas pressures in Wendelstein 7-X during divertor operation under boronized wall conditions

V Haak*, S A Bozhenkov, Y Feng, A Kharwandikar, T Kremeyer, D Naujoks, V Perseo, G Schlisio, U Wenzel and the W7-X Team[1]

Max-Planck-Institut für Plasmaphysik, Greifswald, 17491, Germany

E-mail: victoria.haak@ipp.mpg.de

Received 20 January 2023, revised 16 March 2023
Accepted for publication 30 March 2023
Published 12 April 2023

Abstract

During the first test divertor campaign of the stellarator experiment Wendelstein 7-X (Pedersen *et al* 2022 *Nucl. Fusion* **62** 042022), OP1.2b, 13 neutral gas pressure gauges collected data in different locations in the plasma vessel, enabling a detailed analysis of the neutral gas pressures, the compression ratios and the particle exhaust rates via the turbomolecular pumps in the different magnetic field configurations. In Wendelstein 7-X, the edge magnetic islands are intersected by the divertor target plates and used to create a plasma-wall interface. As the number and position of the magnetic islands varies in different magnetic field configurations, the position of the strike line on the target plates and thus the neutral gas pressure in the subdivertor differs between the configurations. Neutral gas pressures on the order of few 10^{-4} mbar were measured in the subdivertor region. The highest neutral gas pressure of 1.75×10^{-3} mbar was obtained in the so-called high iota configuration featuring four edge magnetic islands per cross section. The neutral particle flux through the pumping gaps into the subdivertor volume was provided by EMC3-EIRENE simulations and allowed to analyze the relation between the particle flux entering the subdivertor and the pressure distribution in the subdivertor. Finite element simulations in ANSYS provide a detailed picture of the pressure distribution in the subdivertor volume and agree with the neutral gas pressure measurements in the subdivertor in the standard configuration featuring an island chain of 5 edge magnetic islands. Surprisingly high neutral gas pressures that were not predicted by the simulation were measured in the subdivertor region away from the main strike line for discharges in the most used magnetic configuration, the standard configuration. While the pressure ratio between the two sections of the subdivertor volume, the low and high iota section is 0.06 in high iota configuration, a ratio of 2–5 was obtained in the other configurations, indicating significant

[1] See Pedersen *et al* 2022 (https://dx.doi.org/10.1088/1741-4326/ac2cf5) for the W7-X Team.
* Author to whom any correspondence should be addressed.

Original Content from this work may be used under the terms of the Creative Commons Attribution 4.0 licence. Any further distribution of this work must maintain attribution to the author(s) and the title of the work, journal citation and DOI.

 © 2023 The Author(s). Published by IOP Publishing Ltd

particle loads and exhaust rates on the high iota section of the subdivertor in magnetic configurations with the main strike line on the low iota divertor targets.

Keywords: Wendelstein 7-X, neutral gas pressure, particle exhaust

(Some figures may appear in colour only in the online journal)

1. Introduction

Wendelstein 7-X [1, 2] is the most advanced stellarator experiment and went into operation in 2015 [3–6]. With a major radius of R = 5.5 m, a minor radius of r = 0.5 m and a plasma volume of 30 m^3, Wendelstein 7-X is, together with LHD [7], the largest operating stellarator. In contrast to the dominating magnetic confinement concept in fusion research, the tokamak, which is based on an external toroidal magnetic field together with a poloidal magnetic field induced by a plasma current [8], the stellarator with its externally generated magnetic field, is not subject to current driven instabilities and pulsed operation, but can be operated continuously, thus providing a prospect for the use of nuclear fusion as an energy source.

In Wendelstein 7-X, heat and particle exhaust is realized by a divertor following the island divertor concept [9–11], which was first explored in the predecessor device Wendelstein 7-AS [12, 13]. The first results using the island divertor concept in Wendelstein 7-X were obtained in operation phase OP1.2a with a test divertor unit consisting of uncooled graphite targets [14], designed for power loads of up to 8 MWm^{-2} [15]. The divertor units are equipped with various diagnostics that allow to explore the properties of the divertor design regarding neutral gas compression and particle exhaust [16, 17].

For the operation of fusion devices, density control is of great importance and can be complicated by particle retention in the wall. The wall accounts for a bound particle reservoir and can act as a dynamic particle source and sink during plasma discharges. It is analyzed by a gas balance based on the different particle sources and sinks, such as the neutral particle content derived from neutral gas pressure measurements [18]. While controlled particle fueling is the first key requirement for density control, the second one is effective particle exhaust, which is determined by the pumping speed of the turbomolecular pumps connected to the subdivertor volume as well as the neutral gas pressure in the subdivertor. Neutral gas pressure measurements in different positions in the plasma vessel, near the pumping gap and in the subdivertor volume are used to assess the efficiency of the divertor to collect and retain neutral particles. Apart from the divertor geometry, particle exhaust in the island divertor can be enhanced by modifying the geometry of the magnetic islands. Changing the size and shape of the islands by applying a control coil current and thus moving the strike line of the plasma closer towards the pumping gap accounts for 30%–50% higher neutral gas pressures in the subdivertor [19].

As the neutral gas pressure in the subdivertor is a key element to characterize particle exhaust and therefore density control in a plasma experiment, the data obtained from neutral gas pressure measurements during the last campaign, OP1.2b, is presented here in detail for the main magnetic configurations used in Wendelstein 7-X. Together with measurements of the recycling flux in front of the pumping gaps of the divertor units and calculations of the particle fluxes through the pumping gaps provided by EMC3-EIRENE, the impact of the divertor geometry on the neutral gas pressure distribution in the subdivertor and thus on the particle removal efficiency can be explored using finite element simulations.

Sections 2 and 3 of the paper give an overview over the divertor geometry and the gas exhaust system in Wendelstein 7-X as well as the neutral gas pressure gauges used for the measurements of the neutral gas pressure.

Section 4 presents the neutral gas pressures obtained in Wendelstein 7-X at different locations in the plasma vessel for different magnetic field configurations and plasma parameters.

In section 5, the distribution of the neutral gas pressure in the subdivertor volume is analyzed in detail for two discharges in standard and high iota magnetic field configuration. The measurements are compared to the results obtained by finite element simulations and analytical calculations, providing a more detailed understanding of the processes involved in neutral gas transport in the subdivertor.

2. Divertor geometry and neutral gas exhaust systems in Wendelstein 7-X

In Wendelstein 7-X, the divertor used for heat and particle exhaust is based on the island divertor concept. The island divertor concept makes use of the magnetic islands present in the edge magnetic field in order to reduce heat and particle load on the divertor targets. The individual divertor units consist of target elements [20–22] intersecting the magnetic islands. The number and location of the island cross sections at a given toroidal location in the plasma vessel is dependent on the rotational transform ι, which measures the number of poloidal turns per toroidal turn of a magnetic field line on a toroidal flux surface. In the different magnetic field configurations, the $\bar{\iota} =$ 5/6 resonance generates 6 intersections of the magnetic island per cross section in the low iota configuration, $\bar{\iota} =$ 5/5 corresponds to 5 in the standard configuration and $\bar{\iota} =$ 5/4 is used to create 4 intersections of the island in the high iota configuration. The divertor consists of an upper and a lower divertor unit in each of the five modules of the plasma vessel, resulting in 10 divertor units in total.

Each divertor unit, as shown in figure 1, consists of a so-called low iota section, middle section and high iota section. The low iota section includes the horizontal and vertical target elements and a set of adjacent baffles [23], the large pumping

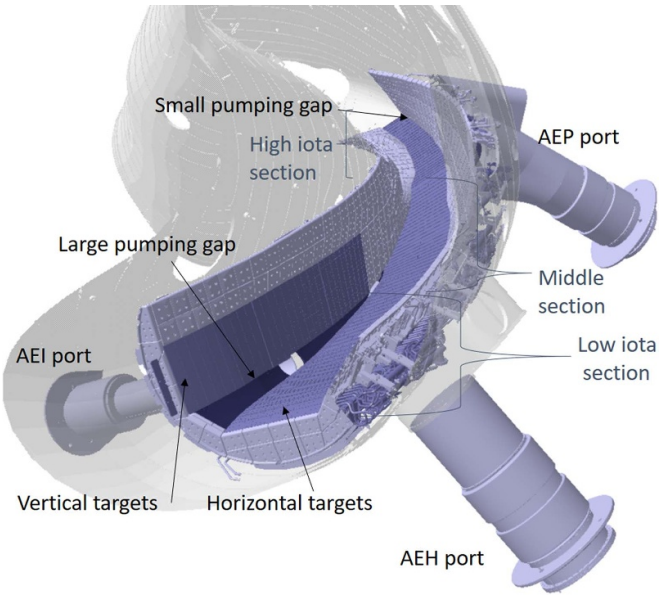

Figure 1. Geometry of one divertor module in Wendelstein 7-X including the pumping ducts at the AEH port and the AEP port, the horizontal and vertical divertor targets and the large and small pumping gap.

gap on the inboard side with a surface area of 0.15 m^2 (from the CAD model) and a pumping duct leading from the AEH port to two turbomolecular pumps. Behind the pumping gap, pumping gap panels [24] are installed for thermal protection of the components in the subdivertor volume. In the high iota section, the small pumping gap with a surface area of 0.06 m^2 is located on the outboard side next to the horizontal target elements. The subdivertor space beneath it is connected to one turbomolecular pump at the AEP port. The subdivertor volume between the low and high iota section of the divertor was separated in operation phase 1 in order to prevent particle exchange between the two volumes.

These two volumes are pumped separately by 3 turbomolecular pumps in total which are operated at 89% of their nominal speed. The two pumps at the AEH port provide an effective pumping speed of 2350 $l\,s^{-1}$ for the low iota subdivertor volume and the pump at the AEP port provides a pumping speed of 1180 $l\,s^{-1}$ for the high iota section of the subdivertor space [25]. The respective pumping ports as well as a part of the subdivertor volume is surrounded by closure plates to prevent particle leakages into other parts of the subdivertor. The closure plates for the high and low iota subdivertor section are shown in figures 2 and 3.

For the next campaign, OP2, each divertor unit will be additionally equipped with a cryopump [26] located below the horizontal target elements in the low iota region of the subdivertor. Each cryopump will provide an additional pumping speed of 60 000 $l\,s^{-1}$ in deuterium [27].

Depending on the magnetic configuration, the strike line can be located on different parts of the target elements, as shown in figure 4. For the low iota and standard configuration, the strike line is located on the low iota section of the divertor near the large pumping gap, resulting in higher particle fluxes

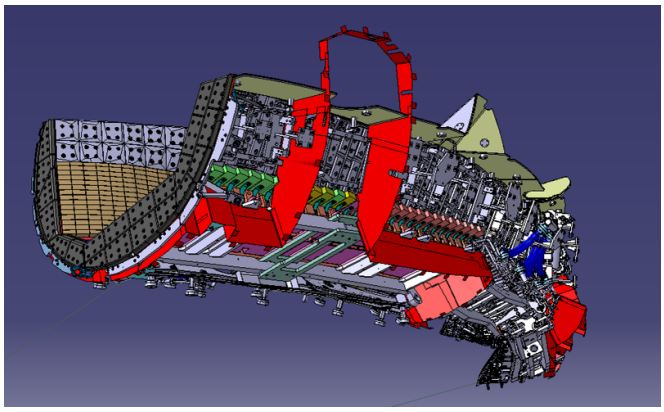

Figure 2. Closure plates around the AEH pumping port.

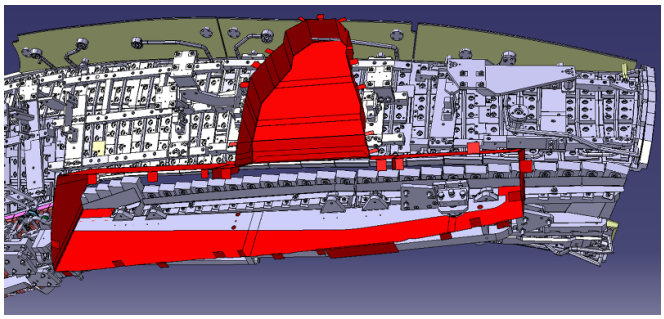

Figure 3. Closure plates around the AEP pumping port.

through the large pumping gap compared to the small pumping gap and a higher neutral gas pressure in the low iota subdivertor volume. For the high iota configuration, the strike line on the horizontal target elements of the high iota section of the divertor leads to higher neutral gas pressures in the high iota section of the subdivertor volume compared to the other magnetic field configurations.

3. Neutral gas pressure gauges at Wendelstein 7-X

In order to characterize the neutral gas pressure at different locations in Wendelstein 7-X, 18 neutral gas pressure gauges were installed for OP1.2b in different positions, including the midplane of the plasma vessel (AEE ports), the large pumping gap in the low iota section of the subdivertor volume (AEI ports), the AEH pumping ports in the low iota section of the subdivertor and the AEP pumping ports in the high iota section of the subdivertor. The different ports in the subdivertor volume are shown in figure 1.

The neutral gas pressure gauges provide an overview over the neutral gas pressure at the different positions, compression ratios, asymmetries of the neutral gas pressure in the different divertor units as well as the rate of particles pumped out of the subdivertor space. ASDEX pressure gauges [29] as well as ionization pressure gauges with a LaB_6-emitter are used. A detailed description of the pressure gauges and the calibration process is given in [17, 30].

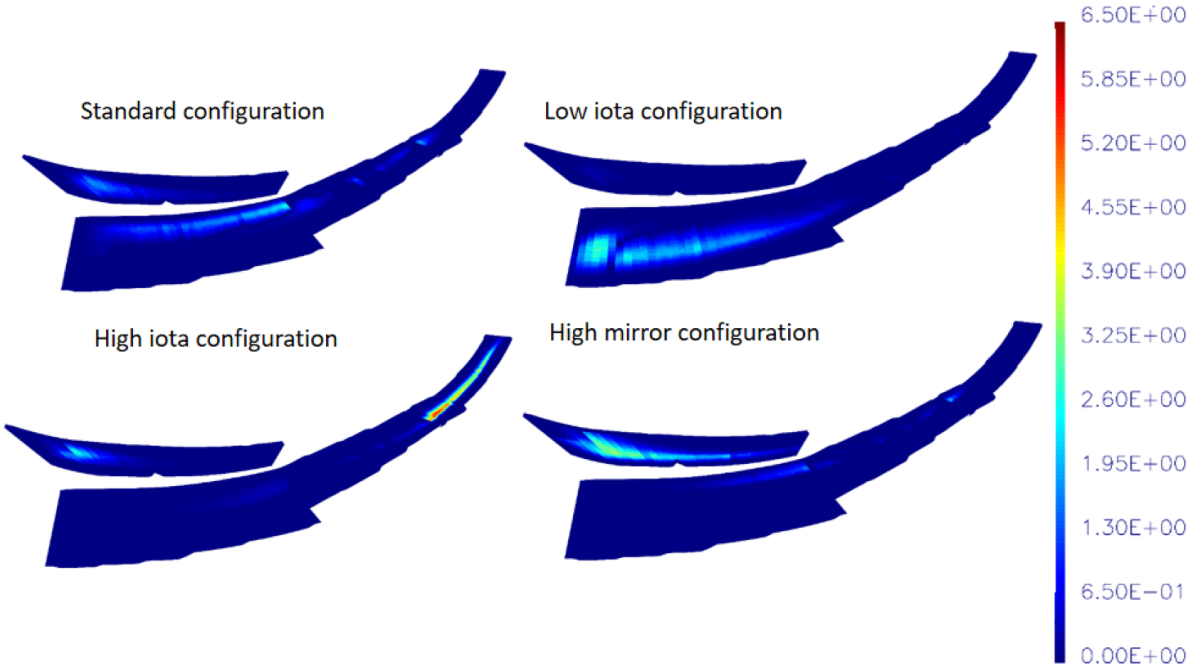

Figure 4. Thermal load on the horizontal and vertical targets of the divertor in standard, low iota, high iota and high mirror configuration in MW m^2 at a density of 5×10^{19} m^{-3} and a heating power of 4.5 MW, modeled with EMC3-Lite [28].

Table 1. Overview over positions in Wendelstein 7-X equipped with neutral gas pressure gauges during OP1.2b.

Module	Divertor unit	AEH port	AEP port	Midplane	Large pumping gap
1	Upper	Yes	No	Yes	No
2	Upper	No	No	No	No
3	Lower	Yes	No	Yes	Yes
3	Upper	Yes	Yes	No	No
4	Upper	Yes	No	Yes	No
5	Lower	No	Yes	No	Yes
5	Upper	Yes	No	No	Yes

The measurements of the neutral gas pressure obtained by the pressure gauges are subject to an uncertainty of 15% [25].

Table 1 provides an overview over the 18 neutral gas pressure gauges initially installed in Wendelstein 7-X during OP1.2b, of which 13 remained functional throughout the whole campaign, whereas five neutral gas pressure gauges with tungsten emitters failed during operation.

4. Neutral gas pressures in Wendelstein 7-X

For controlled fusion in a fusion reactor, density control and particle exhaust are two main requirements for stable operation. As selective exhaust of helium as a fusion product from the neutral gas in the subdivertor is challenging and cannot be provided by turbomolecular pumps as used in Wendelstein 7-X, the necessity to exhaust a sufficient amount of helium increases the required particle exhaust.

The effective pumping speed S_{eff} is determined by the number of pumps installed in the respective device and their nominal pumping speeds S as well as the conductance c of the subdivertor structures to which the pumps are connected and is in general described by

$$\frac{1}{S_{eff}} = \frac{1}{S} + \frac{1}{c}. \tag{1}$$

While the particle exhaust rate is thus limited by the available pumping speed and the location of the pumps with respect to the subdivertor volume, it increases with increasing neutral gas pressure in front of the pumps. Thus, the neutral gas pressure in the subdivertor is a key element for particle exhaust and depends on a variety of different operational and plasma parameters that will be discussed in this section.

The neutral gas pressures obtained in Wendelstein 7-X during OP1.2b are subject to strong variations depending on the magnetic field configuration and the respective location in the subdivertor volume as well as other plasma parameters. An overview over the neutral gas pressures during OP1.2b will be given in this section, while a more detailed explanation of the underlying processes will be given in section 5.

4.1. Neutral gas pressure during attached and detached discharges in different magnetic configurations

While a variety of different magnetic field configurations can be used in Wendelstein 7-X, the majority of the plasma discharges performed during OP1.2b used the standard, high iota, low iota or high mirror magnetic field configuration. As the locations of the magnetic islands with respect to the divertor targets vary in the different magnetic configurations according to the different rotational transforms, the different magnetic field configurations account for different regions of interaction between the plasma and the target modules of the divertor [31]. Simulations of these regions of interaction, the so-called strike lines are shown in figure 4 for the four main magnetic field configurations at a line integrated electron density of 5×10^{19} m^{-2} and a heating power of 4.5 MW, indicating a position of the strike lines closer to the large pumping gap in the standard configuration compared to the low iota and high mirror configuration. As the neutral particles follow a cosine distribution after being neutralized at the target modules, the fraction of the neutralized particles entering the subdivertor volume through the pumping gap depends on the distance of the strike line from the pumping gap.

In the standard configuration as well as the low iota and high mirror configuration, the strike line is mainly located on the target modules in the low iota section. Depending on the specific configuration, it can be located on either the horizontal or the vertical target modules or both. In the high iota configuration, the main strike line is located on the horizontal target modules in the high iota section. Thus, in contrast to the other configurations, where the majority of the particles enters the subdivertor volume through the large pumping gap, in the high iota configuration, more neutral particles pass through the small pumping gap and remain in the high iota section of the subdivertor.

The corresponding neutral gas pressures for these magnetic configurations were measured for a large number of discharges during OP1.2b and are displayed in figure 5 for the AEH pumping ports (low iota part of subdivertor) and in figure 6 for the AEP pumping ports (high iota part of subdivertor) in the subdivertor volume. As there is no pressure gauge installed near the small pumping gap, a comparison of the neutral gas pressures at the pumping gaps would not represent the plasma discharges in the high iota configuration appropriately.

The data points represented in the plots correspond to experiments with electron cyclotron resonance heating (ECRH [32–34]) only, i.e. no neutral beam injection (NBI) and without the use of pellet or impurity injection as well as control coils. Each data point represents an average over 200 ms in a plasma discharge and over the data from neutral gas pressure gauges at different toroidal locations.

In the high iota configuration, the highest neutral gas pressures of up to 1.75×10^{-3} mbar were obtained in the high iota section of the subdivertor, as shown in figure 6. In the other three configurations, the neutral gas pressure is higher at the AEH port compared to the AEP port. Compared to the AEP port in the high iota configuration, lower

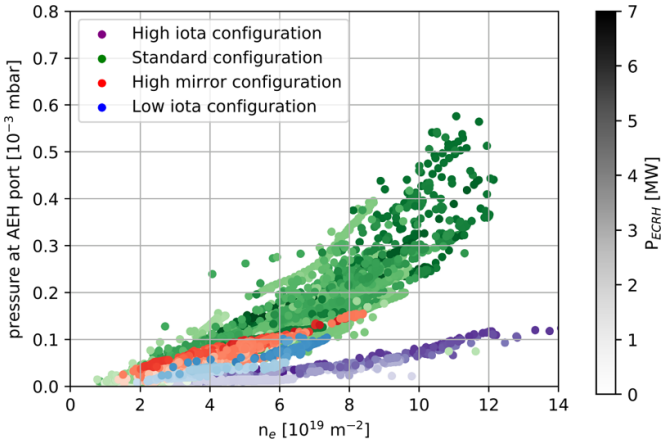

Figure 5. Neutral gas pressure at AEH pumping port (low iota part of subdivertor) for high iota (purple), standard (green), high mirror (red) and low iota configuration (blue) over line integrated electron density, the color intensity of the data points represents the corresponding heating power of up to 7 MW. The variation of the color intensities according to the heating power is indicated in the gray scale on the right.

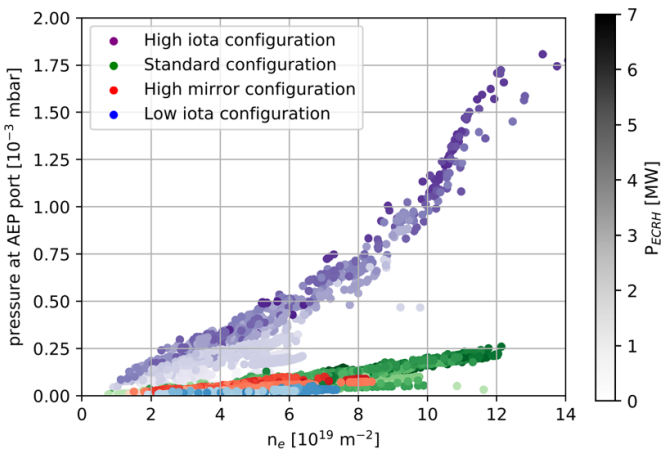

Figure 6. Neutral gas pressure at the AEP pumping port (high iota part of subdivertor) for high iota (purple), standard (green), high mirror (red) and low iota configuration (blue) over line integrated electron density.

neutral gas pressures at the AEH port were measured in the other configurations and are shown in figure 5, i.e. maximum values of 6.00×10^{-4} mbar in the standard configuration, 2.00×10^{-4} mbar in the high mirror configuration and 1.75×10^{-4} mbar in the low iota configuration. The turbomolecular pumps connected to the AEH and AEP ports provide a pumping speed of 2350 l s^{-1} and 1180 l s^{-1} at the ports, which results in a flux of pumped particles per divertor module of up to 1.0×10^{20} a s^{-1} in high iota configuration at the AEP port as well as 6.8×10^{19} a s^{-1} in standard configuration at the AEH port, both at a density of 12×10^{19} m^{-2}, as well as 2.3×10^{19} a s^{-1} in high mirror configuration and 2.0×10^{19} a s^{-1} in low iota configuration at a

density of 8×10^{19} m^{-2} at the AEH port when assuming a temperature of the neutral hydrogen particles of 300 K. While the highest neutral gas pressures are measured at the AEP port in the high iota configuration, the AEP port also accounts for a significant fraction of the exhausted particles even in configurations with the strike line on the low iota section of the divertor and despite the lower pumping speed compared to the AEH port. In the high iota configuration, the neutral gas pressures at the AEH port in the range of up to 1.00×10^{-4} mbar only account for a particle exhaust of 1.1×10^{19} a s^{-1}, which corresponds to 10% of the total exhausted particles. The other 90% are pumped at the AEP port. In the standard configuration, pressures of up to 2.50×10^{-4} mbar at the AEP port lead to 17% of the exhausted particles being pumped at the AEP port. Despite the lower pumping speed at the AEP ports compared to the AEH ports, a significant number of particles is exhausted at the AEP ports due to the higher neutral gas pressure in the high iota section in the subdivertor.

The neutral gas pressure in the subdivertor is strongly influenced by the positions of the magnetic islands and therefore the edge rotational transform [35], which depends on the external magnetic field created by the field coils as well as the magnetic field generated by internal plasma currents. As the bootstrap current, a main contributor to the toroidal plasma current is more dominant in the standard configuration compared to the high iota configuration, larger variations of the toroidal plasma current in the standard configuration lead to significant effects on the position of the strike line. The neutral gas pressure at the AEH ports for the four main magnetic field configurations over the toroidal plasma current is shown in figure 7. With increasing toroidal plasma current, the neutral gas pressure in the low iota section of the subdivertor decreases in the standard configuration as the strike line is moved away from the pumping gap [36] and the neutral particle flux entering the subdivertor through the large pumping gap decreases. In the other magnetic field configurations, the reduction of the neutral gas pressure due to the toroidal plasma current is less significant.

While the fluxes of pumped particles given above for the different magnetic field configurations correspond to the maximum values of the neutral gas pressure in the respective configuration, the neutral gas pressure in the subdivertor and thus the pumped particle flux decrease with decreasing plasma density and vice versa. As the plasma density increases, a higher ion flux towards the divertor targets leads to an increased recycling flux as well as neutral particle flux through the pumping gap into the subdivertor. Due to the increasing heating power required to obtain higher electron densities, the neutral gas pressure increases with the heating power too. Although additional heating by neutral beam injection is used in some discharges, no correlation with the neutral gas pressure has been found.

While the plasma density is the main driver of the neutral gas pressure in the subdivertor, the neutral gas pressure at a given density and heating power differs between attached and detached discharges and depends on the radiated power.

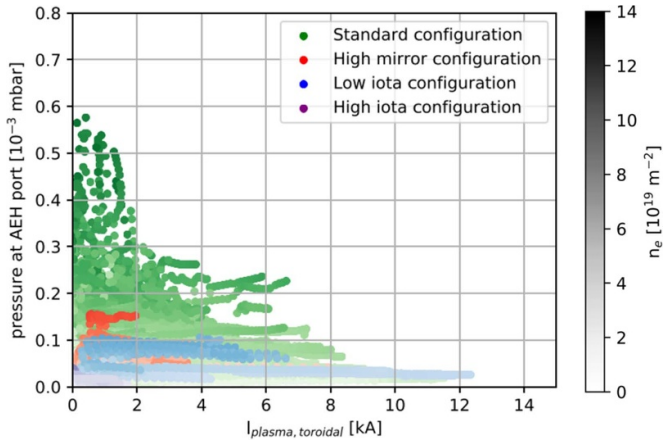

Figure 7. Neutral gas pressure at the AEH pumping port (low iota part of subdivertor) for high iota (purple), standard (green), high mirror (red) and low iota configuration (blue) over toroidal plasma current.

Figure 8 shows the relation between the neutral gas pressure in the subdivertor and f_{rad}, the fraction of the radiated power, which is given by the radiated power divided by the heating power. A reference discharge, program number 20181010.008 is highlighted in order to visualize the evolution of the neutral gas pressure throughout an individual plasma discharge. f_{rad} can be used as a criterion to distinguish attached from detached plasma discharges. In the diagrams shown here, the distinction is made at $f_{rad} = 0.8$, i.e. discharges with $f_{rad} \geqslant 0.8$ are considered detached and discharges with $f_{rad} < 0.8$ are considered attached. For $f_{rad} \geqslant 0.8$, the high radiative losses provide significant reduction of the heat load on the divertor targets, leading to a reduction of the peak heat fluxes from by over 70% from 3 MW m^{-2} to below 0.8 MW m^{-2} [37]. For a more detailed picture of the divertor operation during detached discharges, the reader is referred to [37, 38]. The discharges with 2 MW $< P_{ECRH} \leqslant$ 5 MW are shown on the left and do not show a clear correlation between the neutral gas pressure and f_{rad}. This applies to the discharges with $P_{ECRH} \leqslant$ 2 MW as well, in which the neutral gas pressure does not vary with regard to f_{rad}. Therefore, these discharges are not shown here. For the discharges with more than 5 MW heating power (right figure), the neutral gas pressure increases with increasing f_{rad} in the attached regime as long as $f_{rad} < 0.8$. For $f_{rad} \geqslant 0.8$, the neutral gas pressure stays constant and then decreases slightly as a consequence of the decreasing recycling flux from the divertor targets during detachment [38]. Although the neutral gas pressure in the subdivertor increases during the transition from attached to detached operation, it has to be considered that as detached discharges require higher plasma densities, they do not necessarily lead to an increased fraction of pumped particles from the subdivertor compared to attached discharges. Nevertheless, at a given plasma density, an increase of f_{rad} up to 0.8 leads to increasing neutral gas pressures in the subdivertor and thus facilitates particle exhaust.

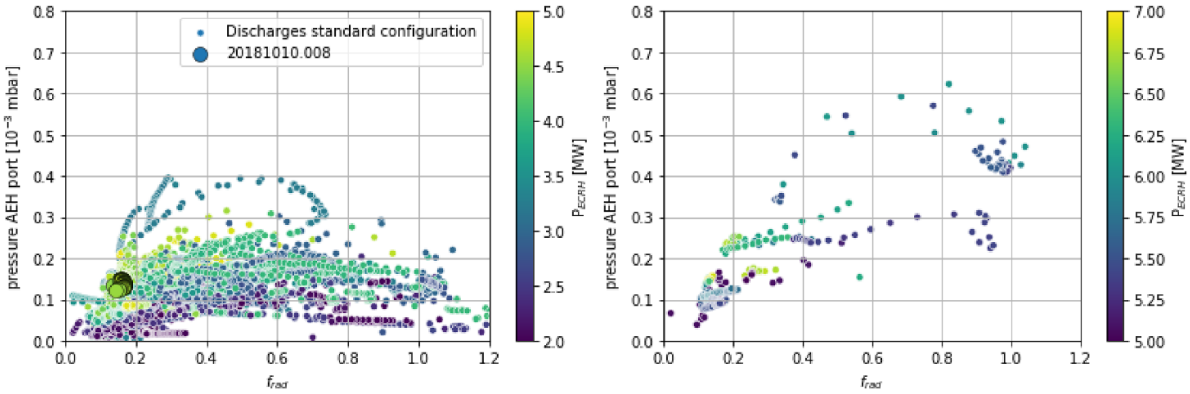

Figure 8. Neutral gas pressure in the standard configuration, measured at AEH port in the low iota part of the subdivertor volume over the fraction of the radiated power f_{rad}, for $2\,\mathrm{MW} < P_{ECRH} \leqslant 5\,\mathrm{MW}$ (left) and $5\,\mathrm{MW} < P_{ECRH} \leqslant 7\,\mathrm{MW}$ (right).

4.2. Neutral gas compression ratios

The compression is defined as the ratio of the neutral gas pressure in the subdivertor and in the midplane, i.e. in the main chamber. The neutral gas in the main chamber consists of neutral gas leaking from the subdivertor back into the main chamber due to leaks in the subdivertor structure as well as a fraction of the particles neutralized at the divertor targets that does not enter the subdivertor through the pumping gap. While the amount of particles exhausted in the subdivertor only depends on the neutral gas pressure in the subdivertor and thus not on the compression ratio, the compression ratio is a useful quantity to assess how much of the neutral particle flux from the recycling zone is collected and retained by the divertor. In addition, higher neutral gas pressures in the main chamber facilitate charge exchange processes and thus cause energy losses in the plasma and fast neutrals that can damage the plasma facing components.

In Wendelstein 7-X, the neutral gas pressure in the midplane of the plasma vessel is measured in module 1, 3 and 4 of the torus (see table 1). The neutral gas pressure in the subdivertor is evaluated at three different locations, i.e. at the AEI ports close to the large pumping gap, at the AEH ports in the low iota section of the subdivertor volume and at the AEP ports in the high iota section of the subdivertor. Due to the lack of neutral gas pressure measurements near the small pumping gap, the compression ratios in the subdivertor, i.e. at the AEH port in the low iota section of the subdivertor volume with respect to the midplane for discharges in standard, high mirror and low iota configuration and at the AEP port in the high iota section for discharges in high iota configuration, are compared for the different configurations in figure 9.

The highest compression ratios at the pumping port are obtained in the high iota configuration with values between 40 and 140. In the standard configuration during attached discharges, values of up to 70 and slightly lower values of up to 40 and 30 are obtained in the high mirror and low iota configuration, respectively. Similar compression ratios have been measured in other plasma experiments such as Alcator C-Mod with compression ratios of up to 70 [39] or ASDEX Upgrade with compression ratios around 30 with the original divertor

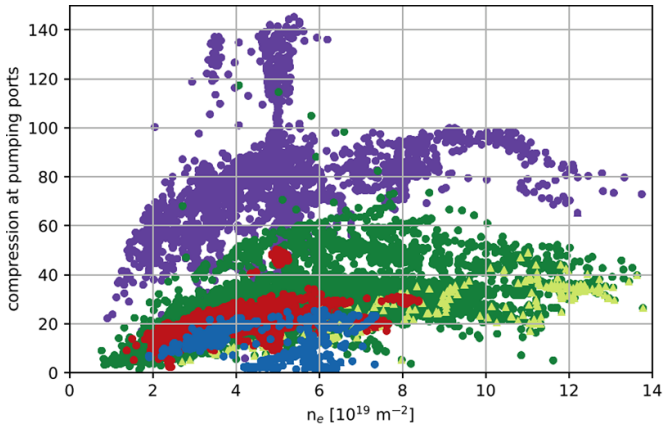

Figure 9. Compression ratio at the pumping ports (AEP port for high iota configuration and AEH port for standard, high mirror and low iota configuration) of the subdivertor with respect to the midplane (AEE) for high iota configuration (purple), attached (green circles) and detached (light green triangles) discharges in standard configuration, high mirror (red) and low iota configuration (blue) over line integrated electron density.

and up to 180 with the lyra divertor configuration [40]. The compression ratios in the standard and high iota configuration show the largest variation due to the wide range of parameters covered during discharges in the these configuration, which were the most frequently used configurations during OP1.2b. Although detached discharges, which are highlighted in light green in figure 9, usually result in a higher neutral gas pressure in the subdivertor compared to attached discharges, the compression ratio is lower in the detached discharges in standard configuration compared to the attached discharges, which is due to higher midplane pressures during detached discharges. Although neutral gas pressure and thus particle exhaust is not necessarily affected by lower compression ratios in this case and even shows a tendency to increase during the transition to detachment compared to attached plasma conditions at the same plasma density, the higher neutral gas pressures in the main chamber are not desirable as they account for energy losses by charge exchange recombination and fast neutrals.

A degradation of the compression ratios at high densities and during the transition to detachment has been observed in other plasma experiments like LHD [41] and Alcator C-Mod [39] too.

The compression ratios in the high iota configuration are about twice as high as in the standard configuration, which applies to the neutral gas pressures at the AEP and AEH port in the respective configurations as well, indicating similar neutral gas pressures in the midplane in both, high iota and standard configuration. Therefore, at a given midplane pressure, higher neutral gas pressures in the subdivertor are obtained in the high iota configuration compared to the standard configuration, resulting in increased particle exhaust at the AEP port compared to the standard configuration without a potential increase in energy losses and damages to the plasma facing components caused by higher midplane pressures.

5. Variation of the neutral gas pressure in the subdivertor

As the flux of exhausted particles linearly depends on the neutral gas pressure in front of the pumps for a given configuration of turbomolecular pumps, high neutral gas pressures in the subdivertor volume are essential. As particles are exhausted at both, the AEH and the AEP port, the distribution of the neutral gas pressure in the subdivertor volume and, in particular, at locations of the pumps is of interest. Apart from the neutral particle flux through the pumping gaps into the subdivertor, the neutral gas pressure in the low and high iota section of the subdivertor and thus the particle exhaust depend on the geometry of the subdivertor space, i.e. the conductances between the pumping gaps and the locations of the pumps as well as the area of the leaks allowing for neutral gas to leak back into the main chamber. As higher neutral gas pressures have been obtained in the high iota section of the subdivertor compared to the low iota section, the two sections will be compared with regard to the aforementioned criteria.

Two discharges in the standard and high iota configuration will be analyzed with respect to the distribution of the neutral gas pressure in the low and high iota section of the subdivertor volume, i.e. at the AEH and AEP pumping ports where measurements of the neutral gas pressure are available. The experimental data is complemented by an analytical estimate for the steady state neutral gas pressure in the low and high iota section of the subdivertor. Finite element simulations provide the distribution of the neutral gas pressure across the whole subdivertor module and are presented for a more detailed understanding of the processes controlling the distribution of the neutral gas pressure in the subdivertor. The neutral particle fluxes into the subdivertor through the pumping gaps are provided by EMC3-EIRENE simulations as an input for the finite element calculations.

5.1. Distribution of the neutral gas pressure in the subdivertor in the standard and high iota configuration

Figure 10 shows the pressure ratio between the AEH (low iota part of subdivertor) and the AEP port (high iota part of subdivertor) for the four different magnetic configurations. The ratio is lowest in the high iota configuration with values around 0.06, which is expected considering that most particles enter the subdivertor volume through the small pumping gap in the high iota section of the divertor. In the high iota configuration, fewer particles enter the low iota section of the subdivertor, yielding smaller neutral gas pressures at the AEP port and a smaller AEH/AEP ratio compared to the other magnetic field configurations.

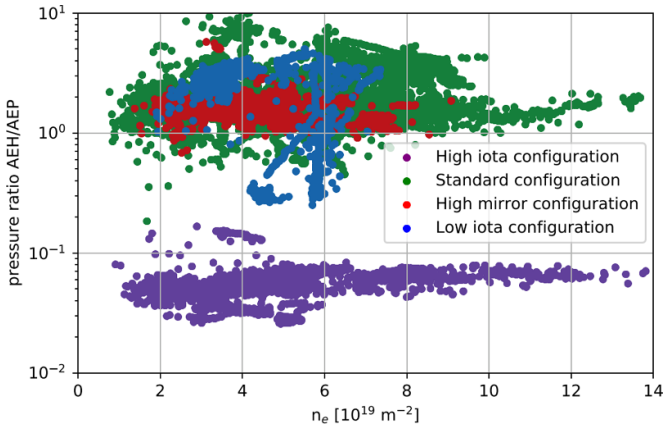

Figure 10. Ratio of the neutral gas pressure at the AEH port (low iota part of subdivertor) and AEP port (high iota part of subdivertor) in standard, high iota, high mirror and low iota configuration over line integrated electron density.

In the standard and high mirror configuration, the neutral gas pressure in the low iota section of the subdivertor as measured at the AEH port is around twice as high as in the high iota section. In the low iota configuration, the ratio is slightly larger at around 3–5. Considering that in these configurations, the strike line is located almost entirely on the target modules in the low iota section, i.e. near the large pumping gap, a remarkably high neutral gas pressure is still obtained at the AEP port, allowing for significant particle exhaust rates at the AEP ports.

In order to investigate the high neutral gas pressure in the high iota section of the subdivertor in more detail, two similar plasma discharges in the standard (20181010.008) and high iota configuration (20180904.031) have been selected for comparison. They were performed at medium line integrated electron densities of 6×10^{19} m^{-2} in the standard and 5×10^{19} m^{-2} in the high iota configuration and used 4.5 MW and 4 MW of ECRH power, respectively. The neutral gas pressures measured at the different locations in the subdivertor during both discharges are given in table 2.

5.2. Particle flux through the large and small pumping gap into the low iota and high iota section of the subdivertor

5.2.1. Particle fluxes calculated by EMC3-EIRENE. As recycling of the plasma particles occurs on the target modules of the divertor close to the large and small pumping gap, a fraction of the neutral particles enters the subdivertor volume through one of the pumping gaps. This fraction of the ion flux acts as the main source of the neutral gas pressure

Table 2. Mean neutral gas pressure at the large pumping gap (AEI), in the low iota section of the subdivertor volume (AEH) and in the high iota section of the subdivertor volume (AEP) during discharge 20181010.008 and 20180904.031.

Discharge	Pressure AEI port (mbar)	Pressure AEH port (mbar)	Pressure AEP port (mbar)
Standard configuration (20181010.008)	2.6×10^{-4}	1.4×10^{-4}	8.2×10^{-5}
High iota configuration (20180904.031)	3.5×10^{-5}	2.4×10^{-5}	4.1×10^{-4}

Table 3. Neutral particle flux through the large and small pumping gap for discharge 20181010.008 and 20180904.031, calculated using EMC3-EIRENE.

Discharge	Particle flux through large pumping gap (atoms s^{-1})	Particle flux through small pumping gap (atoms s^{-1})
Standard configuration (20181010.008)	3.23×10^{20}	2.66×10^{19}
High iota configuration (20180904.031)	1.15×10^{20}	2.78×10^{20}

in the low and high iota section of the subdivertor, where part of it is exhausted by the turbomolecular pumps. In order to investigate the relation between the neutral particle flux through the pumping gaps and the neutral gas pressure in the subdivertor volume, the neutral particle flux through the large pumping gap into the low iota section of the divertor as well as through the small pumping gap into the high iota section of the divertor was calculated by means of the EMC3-EIRENE simulation [42–44] and is presented in table 3.

For discharge 20181010.008 in standard configuration, the EMC3-EIRENE simulation results in a particle flux through the large pumping gap of 3.23×10^{20} atoms s^{-1}, which is twelve times as large as the particle flux through the small pumping gap with 2.66×10^{19} atoms s^{-1}. For discharge 20180904.031 in high iota configuration, 1.15×10^{20} atoms s^{-1} enter the subdivertor through the large pumping gap and 2.78×10^{20} atoms s^{-1} through the small pumping gap, yielding a ratio of 0.4.

Comparing the ratios of particles entering through the pumping gaps to the ratio of the neutral gas pressure in the low and high iota section of the subdivertor given in the previous section ($p_{AEH}/p_{AEP} = 1.7$ for standard and 0.06 for high iota configuration) indicates that the neutral gas pressure in the subdivertor is not exclusively dependent on the particles flux through the pumping gaps and the subdivertor volume, but is also strongly influenced by the divertor geometry.

The geometry of the low iota and high iota section of the subdivertor is shown in figure 11. In the standard configuration, the strike line is located mainly on the horizontal target modules in the low iota section of the divertor. Those targets form the main recycling surfaces [45]. The recycled particles are emitted from the target modules according to the cosine distribution. The majority of the particles is emitted towards the main chamber again, whereas only a small fraction enters through the large pumping gap. The pumping gap panels that are installed to protect the components in the subdivertor volume from thermal loads are located beneath the large pumping gap and reflect a fraction of the incoming particles back into the main chamber.

In the high iota configuration, the strike line is located on the target modules in the high iota section of the divertor, where no pumping gap panels are installed. Due to the smaller angle of 120.7° between the small pumping gap and the target modules, the fraction of the recycled particles entering the subdivertor through the pumping gap is higher than in the low iota section, where the respective angle is 137.7°. In addition, there are no losses of particles due to reflection at the pumping gap panels.

Although twelve times as many particles enter the subdivertor through the large pumping gap compared to the small pumping gap in the standard configuration according to EMC3-EIRENE modeling, the neutral gas pressure in the low iota section is only by a factor of 1.7 higher than in the high iota section, which is due to the less beneficial geometry of the divertor in the low iota section.

5.2.2. H_α-measurements of the recycling flux. Experimental verification of the particle fluxes calculated by EMC3-EIRENE can be approximated by H_α-measurements in front of the target modules. The Balmer alpha line can be detected by optical emission spectroscopy, where the photon flow generated by the signal corresponds to the total flow of neutrals that re-ionize after recycling [46]. The conversion from the photon flux to the flux of neutrals can be done using effective S/XB coefficients, but is not carried out here for reasons of simplicity.

As most particles from the divertor ionize within a short distance above their recycling surface, H_α-measurements can be used to estimate the recycling flux at the position of the strike line. The fraction of the recycling flux that enters the subdivertor through the pumping gap cannot directly be determined from the measurements, which serve as an estimate of the particle loads on the different parts of the divertor here, but can be assumed to be proportional to it. The different zones in which the target modules are divided for the data analysis are shown in figure 12. For our purposes, the low iota and high iota zone are of interest, as most of the recycling occurs in these zones. It is shown in figure 12 that, however, only minor re-ionization of neutral particles of about 7% occurs near the baffles and negligible re-ionization on the heat shield. The recycling flux emitted from the middle part of the target modules is significantly lower than in the low and high iota zone.

For discharge 20181010.008, the ratio of the photon flux between the low iota and the high iota zone, which is treated as an equivalent to the ratio of neutral particles entering

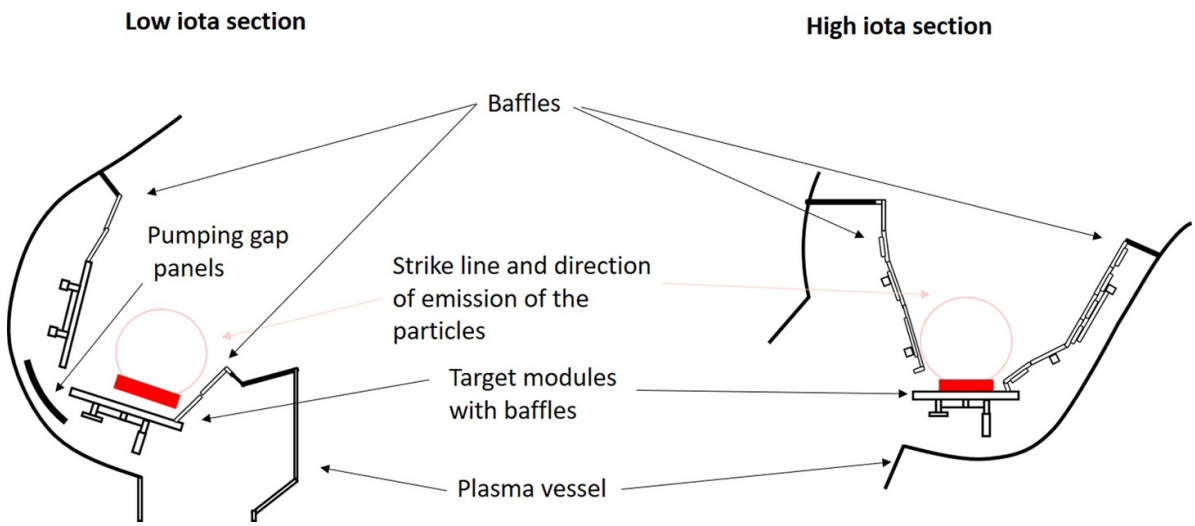

Figure 11. Schematic cross section of the low iota and high iota section of the subdivertor volume including target modules, baffles, strike line on the target modules and direction of emission of the neutralized particles according to the cosine distribution. The pumping gap panels in the low iota section are indicated in black.

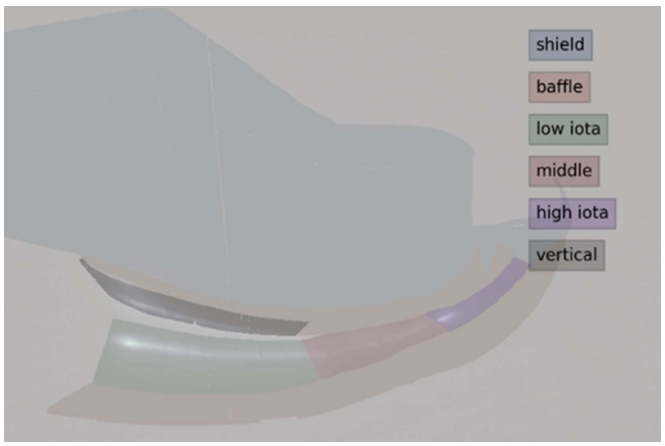

Figure 12. Locations of the different areas on the divertor used for the analysis of the H_α-data for discharge 20181010.008.

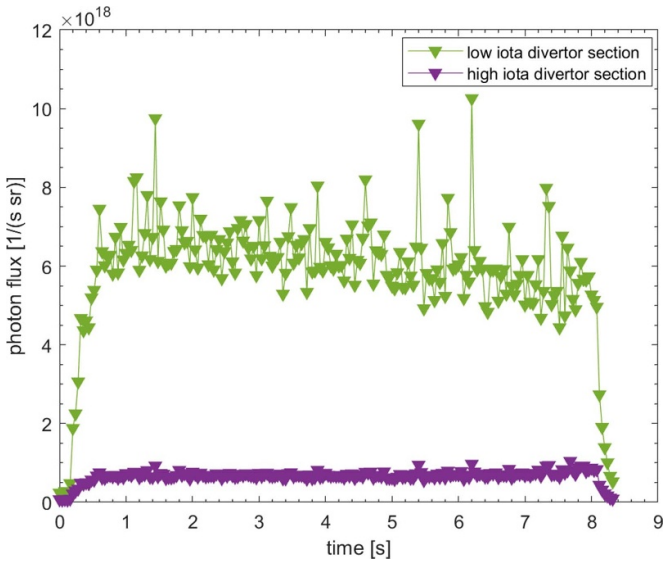

Figure 13. Integrated photon flux from the low and high iota section of the divertor targets obtained by H_α-measurements for discharge 20181010.008, module 1, upper divertor.

the subdivertor through the large and small pumping gap, is ≈7 (see figure 13), compared to a ratio of 12 provided by EMC3-EIRENE. For the discharge 20180904.031 in high iota configuration, a photon flux ratio of 0.5 between the low and high iota zone was obtained (see figure 14), compared to the ratio of 0.4 provided by EMC3-EIRENE. It is also visible in figure 15 that the recycling almost exclusively occurs on the target modules in the high iota section in the high iota configuration, whereas the main recycling zone is located on the target modules in the low iota section of the divertor in the standard configuration (see figure 12).

5.3. Finite element simulations of the neutral gas pressure in the subdivertor volume using ANSYS

While consistent ratios of the particle flux into the low and high iota section of the subdivertor have been obtained by the EMC3-EIRENE simulation and the H_α-measurements, the ratio of the neutral gas pressures measured at the AEH and AEP port (see table 2) differs from the results obtained from EMC3-EIRENE and H_α-measurements by a factor of ≈7 for both configurations. As the particle flux through the pumping gaps does not seem to fully account for the pressure distribution in the subdivertor, finite element simulations for the distribution of the neutral gas pressure in the subdivertor have been carried out in ANSYS for a reduced geometry of one divertor module for both reference discharges. These simulations allow for a more detailed study of the influence of the divertor geometry on the distribution of the neutral gas pressure.

In the pressure range obtained in the subdivertor of Wendelstein 7-X during OP1.2b, the molecular regime is dominant, i.e. the mean free path of the neutral particles is long enough

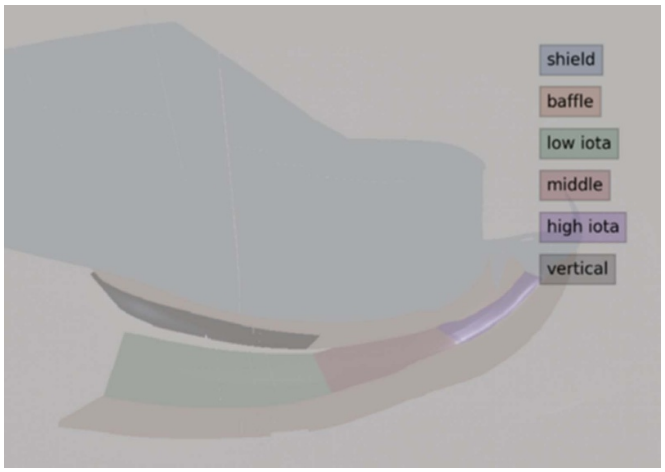

Figure 14. Locations of the different areas on the divertor used for the analysis of the H_α-data for discharge 20180904.031.

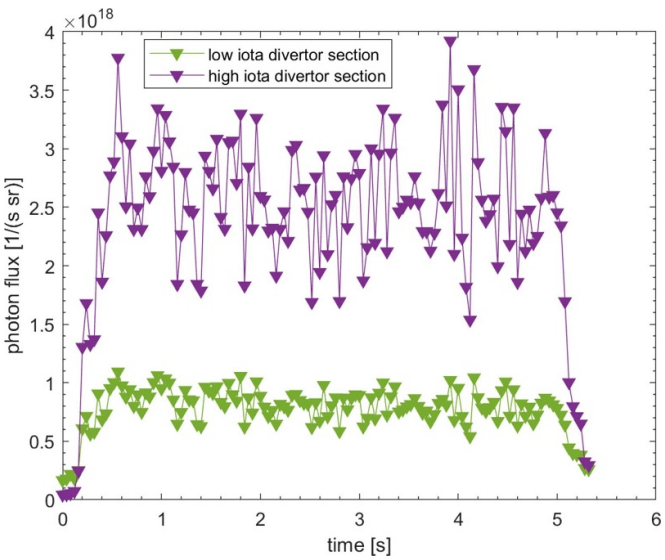

Figure 15. Integrated photon flux from the low and high iota section of the divertor targets obtained by H_α-measurements for discharge 20180904.031, module 1, upper divertor.

that collisions between the particles do not play a significant role compared to interactions of the particles with the walls. Therefore, their dynamics and transport are computationally identical to those of photons. Advantage can be taken of this similarity by using the ANSYS steady-state thermal package, which simulates photon emission and reflection from material components for three dimensional geometries, to emulate the dynamics of the neutral gas particles in the subdivertor.

The properties that can be assigned to the geometric surfaces in the simulation are the temperature T and the emissivity ϵ. Fully reflecting surfaces that do not release particles are represented with a temperature of $T = 0$ K and an emissivity of $\epsilon = 0$. Surfaces that absorb particles such as the turbomolecular pumps can be represented using $T = 0$ K and $0 < \epsilon < 1$, where ϵ is determined by the pumping speed. The pumping gaps that act as a net source of particles for the subdivertor volume, are treated as radiating surfaces ($0 < \epsilon < 1$) with a finite temperature $T > 0$ K, which makes them emit photons by virtue of the blackbody formula embedded in the code.

The thermal load on the components as calculated by the code is linked to the neutral gas pressure by a scaling factor. The temperature of the surfaces in ANSYS is denoted by T whereas the actual temperature of the neutral gas is denoted T_n. The scaling factor is defined as

$$s_f = \frac{\Phi_p \sqrt{2k_B T_n \pi m}}{A\epsilon\sigma T^4}, \tag{2}$$

A is the area of the pumping gap (0.15 m^2 for the large pumping gap and 0.06 m^2 for the small pumping gap), T the temperature of the pumping gaps in the simulation, T_n the temperature of the neutral gas particles (300 K) and Φ the particle flux through the pumping gaps, which is provided by EMC3-EIRENE simulations. A scaling factor of 6.0679×10^8 mbar/W m^2 is used and chosen such that for the range of expected particle fluxes Φ, the pumping gap temperatures are kept above 100 K for reasons of numerical stability and below 800 K to reduce computing time. Adjusting the temperatures of the pumping gaps to the given particle flux and the scaling factor yields the values given in table 4.

The simulation results for discharge 20181010.008 in standard configuration show a maximum pressure of 1.4×10^{-4} mbar near the large pumping gap and a pressure of 1.0×10^{-4} mbar at the AEH pumping port, which is slightly lower than the average pressure measured by the pressure gauges in the different AEH ports of 1.4×10^{-4} mbar (see table 2). The overall pressure distribution in one divertor unit is shown in figure 16. At the AEP port, the simulation results in a neutral gas pressure of 4.0×10^{-5} mbar, compared to 8.2×10^{-5} mbar measured by the neutral pressure gauges in the AEP ports and thus has a larger deviation from the experimental results than at the AEH port in the low iota section of the subdivertor.

The simulation for the high iota discharge, 20180904.031, results in the pressure distribution given in figure 17 and shows a maximum neutral gas pressure of 1.0×10^{-4} mbar near the small pumping gap and a pressure of 9.0×10^{-5} mbar at the AEP port. These values differ from the measurements of the neutral gas pressure gauges in the AEP position, which account for a pressure of 4.1×10^{-4} mbar. The neutral gas pressure at the AEH port of 4.6×10^{-5} mbar in the simulation differs from the measurement of 2.4×10^{-5} mbar by a factor of 2.

For both discharges, especially the results of the neutral gas pressure in the high iota section are a factor of 2 in standard and a factor of 4.5 in high iota configuration smaller than the mean neutral gas pressure measured at the AEP port during the discharges, which is due to the simplified geometry used for the simulation. As shown in figures 2 and 3, both sections of the subdivertor have been equipped with custom-made closure plates that are not included in CATIA and thus cannot be taken into account in the simulation. Therefore, the exact volume accessible for the neutral gas entering through the pumping gap is unknown for both sections of the subdivertor. The deviation of the simulation results from the measurements

Table 4. Particle flux through the large pumping gap into the low iota section of the subdivertor and through the small pumping gap into the high iota section of the subdivertor according to EMC3-EIRENE and corresponding temperatures in the ANSYS simulation for discharge 20181010.008 and 20180904.031.

Discharge	Particle flux through large pumping gap (atoms s^{-1})	Temperature large pumping gap (K)	Particle flux through small pumping gap (atoms s^{-1})	Temperature small pumping gap (K)
Standard configuration (20181010.008)	3.23×10^{-20}	452.3	2.66×10^{-19}	242.3
High iota configuration (20180904.031)	1.15×10^{-20}	349.4	2.78×10^{-20}	435.7

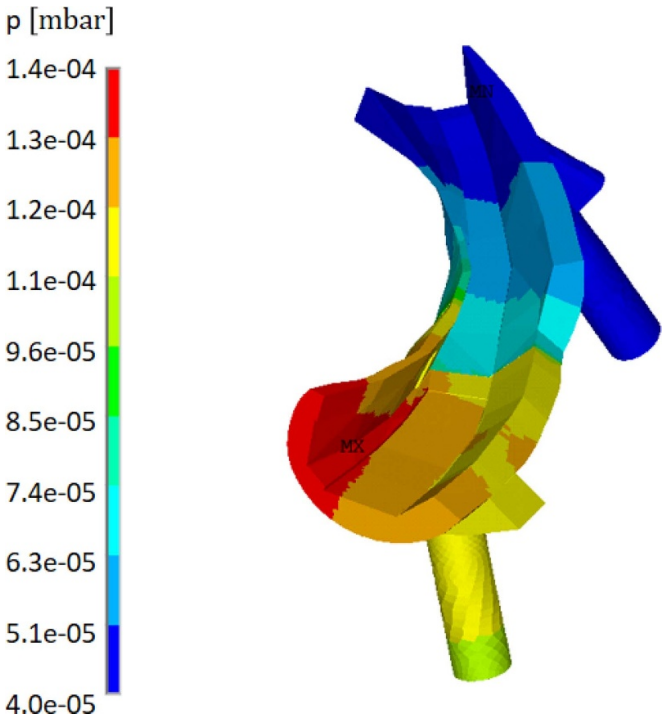

Figure 16. Finite element simulation of the neutral gas pressure in the subdivertor for the discharge in standard configuration (20181010.008).

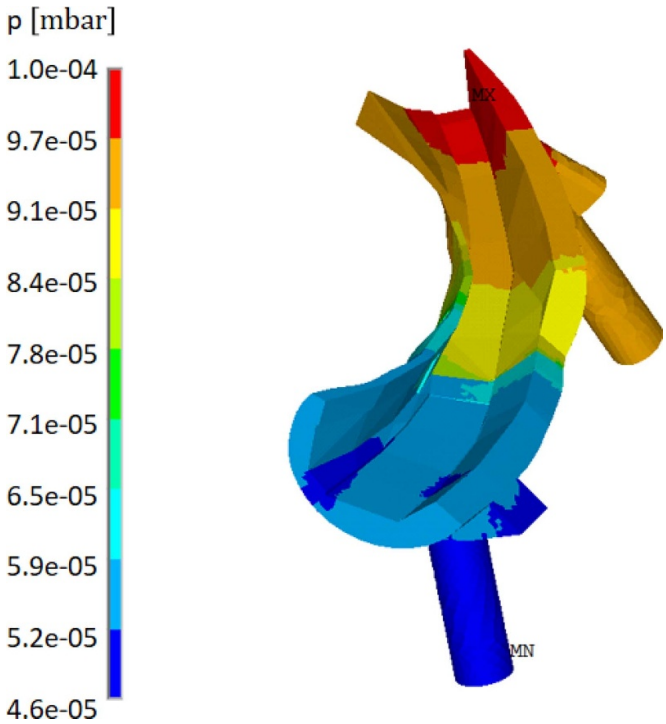

Figure 17. Finite element simulation of the neutral gas pressure in the subdivertor for the discharge in high iota configuration (20180904.031).

for the high iota section indicates that especially in the high iota section, the volume accessible for the neutral gas is restricted significantly by the closure plates compared to the total volume of the high iota section. Due to the reduced effective subdivertor volume, the closure plates also restrict the number and area of leaks contributing to the loss of neutral particles from the subdivertor back into the main chamber, which cannot be taken into account in the simulation without and accurate representation of the closure plates.

Besides the limitations of the simulation results due to the accuracy of the geometry used for the calculation, the underlying principle of the simulation inherently limits the calculations to particles in the molecular flow regime. While the mean free paths of the hydrogen molecules at room temperature of 0.75 m for a neutral gas pressure of 1.4×10^{-4} mbar in the low iota section during discharge 20181010.008 and 0.28 m for a neutral gas pressure of 4×10^{-4} mbar in the high iota section during discharge 20180904.031 are still below the characteristic length of the subdivertor structures in the respective section of the subdivertor, larger differences between the simulation results and measurements have to be expected for increasing neutral gas pressures, because the collisions between particles cannot be accounted for in the code.

5.4. Estimate of the neutral gas pressure in the low and high iota section of the subdivertor using a conductance model

A simple analytical model for the steady-state neutral gas pressure in the low and high iota section of the subdivertor can be used to verify the simulation results [47, 48]. As the low iota and high iota section of the subdivertor were separated from each other during OP1.2b such that only negligible particle exchange between the two volumes occurred, they

Table 5. Steady-state pressure in the low and high iota section of the subdivertor volume and corresponding pressure measurements at the AEH and AEP port for discharge 20181010.008 and 20180904.031.

Discharge	Calculated pressure low iota subdivertor section (mbar)	Measured pressure AEH (mbar)	Calculated pressure high iota subdivertor section (mbar)	Measured pressure AEP (mbar)
20181010.008	$1.3(\pm 0.4)\times 10^{-4}$ mbar	1.4×10^{-4} mbar	$4.1(\pm 1.6)\times 10^{-5}$ mbar	8.2×10^{-5} mbar
20180904.031	$1.8(\pm 0.6)\times 10^{-5}$ mbar	2.4×10^{-5} mbar	$1.6(\pm 0.6)\times 10^{-4}$ mbar	4.1×10^{-4} mbar

can be treated independently. The pressure balance for each unit,

$$\frac{dp}{dt} = -\frac{S_{eff}(p)}{V}\cdot p + \frac{q_{pv}}{V} - \frac{q_{pv}^{loss}}{V}, \tag{3}$$

has to be solved for the steady-state case. It takes into account the particle sinks created by the turbomolecular pumps, which are represented by the effective pumping speed S_{eff} of 2350 $\mathrm{l\,s^{-1}}$ for the low iota section of the subdivertor and 1180 $\mathrm{l\,s^{-1}}$ for the high iota section, as well as the leaks in the subdivertor structures allowing for particles to move back into the main chamber, which is represented by q_{pv}^{loss}. For both subdivertor units, the particle flux through the pumping gap q_{pv} into the subdivertor volume acts as a source term. V is the volume of the respective subdivertor section.

For the steady-state case, the equation for the pressure in the subdivertor reads

$$p_{subdiv} = (q_{pv} - q_{pv}^{loss})\cdot\frac{1}{S_{eff}(p)}. \tag{4}$$

Replacing q_{pv} and q_{pv}^{loss} using the ideal gas equation and

$$\frac{dN}{dt} = \frac{1}{4}nv_{th}A_{pg} = \sqrt{\frac{k_BT_{H_2}}{2\pi\, m_{H_2}}}nA_{pg}, \tag{5}$$

with N being the number of particles, here hydrogen molecules, m_{H_2} the mass of a hydrogen molecule and v_{th} the thermal velocity of the hydrogen molecules, yields

$$p_{subdiv} = (n_{div}A_{pg}(k_BT_{H_2}^{div})^{\frac{3}{2}} - n_{subdiv}A_{leak}(k_BT_{H_2}^{subdiv})^{\frac{3}{2}})\cdot\frac{1}{\sqrt{2\pi m_{H_2}}S_{eff}(p)} \tag{6}$$

$$= \frac{A_{pg}p_{div}\sqrt{k_BT_{H_2}^{div}}}{\sqrt{2\pi m_{H_2}}S_{eff}(p) + A_{leak}\sqrt{k_BT_{H_2}^{subdiv}}}, \tag{7}$$

with $T_{H_2}^{subdiv} = T_{H_2}^{div} = 300$ K being the temperature and n_{div} as well as n_{subdiv} being the density of the hydrogen molecules in the divertor and subdivertor, A_{pg} being the surface area of the pumping gap, which is 0.15 $\mathrm{m^2}$ for the large pumping gap and 0.06 $\mathrm{m^2}$ for the small pumping gap, A_{leak} being the area of the leaks with 0.30 $\mathrm{m^2}$ for the low iota section and 0.22 $\mathrm{m^2}$ for the high iota section of the subdivertor, as extracted from the simplified geometry used in ANSYS, and p_{div} being the pressure at the entrance to the subdivertor. For the low iota section of the divertor, the mean pressure measured at the AEI port near the large pumping gap can be used, which is 2.6×10^{-4} mbar during discharge 20181010.008 and 3.5×10^{-5} mbar during discharge 20180904.031. For the pressure at the small pumping gap in the high iota section of the divertor, there is no measurement available. When assuming that $\frac{p_{\mathrm{AEH}}}{p_{\mathrm{AEI}}} = \frac{p_{\mathrm{AEP}}}{p_{\mathrm{small\ pumping\ gap}}}$, the pressure near the small pumping gap can be calculated for both discharges and is 1.5×10^{-4} mbar for discharge 20181010.008 and 5.9×10^{-4} mbar for discharge 20180904.031.

The pressure in the two sections of the subdivertor as calculated according to equation (6) is given in table 5.

Among the quantities in equation (6), especially p_{div}, which is measured by the neutral gas pressure gauges in case of the low iota section and estimated according to these measurements for the high iota section is subject to substantial uncertainty as well as A_{leak}. For OP1.2b, the subdivertor volume near the AEH (see figure 2) and AEP (see figure 3) pumping ports was surrounded by closure plates in order to provide more effective pumping. As in the ANSYS model, neither the subdivertor volume nor the leakage area given here take into account the closure plates. Especially in the high iota section of the subdivertor, the volume surrounded by the closure plates is small and therefore the leakage area is expected to be significantly smaller than in the simplified model, in which the leakage area in the high iota section is as large as 75% of the leakage area in the low iota section, while the volume of the high iota section is only about 10% of the volume of the low iota subdivertor section.

For the measurements of the neutral gas pressure, an uncertainty of 15% is given in [25, 30]. Due to the complexity of the geometry, the uncertainty of the leakage area is not known precisely, but is estimated to be 20% here. Assuming that the pumping speed and the pumping gap areas are known, the total uncertainty is given by

$$\Delta p = \left|\frac{dp_{subdiv}}{dp_{div}}\right|\cdot\Delta p_{div} + \left|\frac{dp_{subdiv}}{dA_{leak}}\right|\cdot\Delta A_{leak} \tag{8}$$

$$= \frac{A_{pg}\cdot\sqrt{k_BT_{H_2}^{div}}}{\sqrt{2\pi\, m_{H_2}}S_{eff}(p) + A_{leak}\sqrt{k_BT_{H_2}^{subdiv}}}\cdot\Delta p_{div} + \frac{A_{pg}\cdot p_{div}\cdot k_BT_{H_2}^{div}}{\left(\sqrt{2\pi\, m_{H_2}}S_{eff}(p) + A_{leak}\sqrt{k_BT_{H_2}^{subdiv}}\right)^2}\cdot\Delta A_{leak}, \tag{9}$$

and indicated in brackets in table 5 for the respective results.

For both configurations, the neutral gas pressure measured at the AEH port in the low iota section of the subdivertor

is within the uncertainty of the pressure calculated using a steady-state pressure balance for both discharges. Although no uncertainty can be given for the simulation results obtained with ANSYS, the results are in good agreement with the measurements in the low iota section of the subdivertor. For the high iota section of the subdivertor, the results of the simulation and the steady-state estimate given here differ from the neutral gas pressure measured in the AEP port by a factor of 2. For both configurations, the pressure measured at the AEP port is larger than the one predicted by the ANSYS simulation or the analytical model, which can be attributed to the following two factors. First, the exact leakage area in both, the low and high iota section of the subdivertor are unknown. Second, there is no pressure measurement available in front of the small pumping gap. Therefore, the pressure has to be estimated assuming that the relation between the pressure at the small pumping gap and at the AEP port is similar to the relation of the pressure near the large pumping gap and at the AEH port. The geometric differences between the low and high iota section of the subdivertor as well as the position of the strike line on the target modules of the low and high iota section with respect to the pumping gaps are not taken into account here. Therefore, the uncertainty concerning the pressure in front of the pumping gap is significantly higher for the high iota section than for the low iota section, resulting in a larger variation of the neutral gas pressures obtained by measurements, simulation and analytical calculations.

6. Summary

In a plasma experiment as well as in a future fusion device, controlled gas exhaust is necessary for density control as well as sufficient exhaust of the fusion product helium. The particle exhaust is determined by the available pumping capacity, the conductances of the subdivertor structures and the neutral gas pressure in front of the pumps. For the next campaign, OP2, the newly installed cryopump in Wendelstein 7-X will provide an additional pumping speed of 60 000 $\mathrm{l\,s^{-1}}$ and thus increase the total pumping capacity by 170%. As the geometry of the divertor cannot be changed easily, the main factor determining gas exhaust, apart from the pumping capacity, is the neutral gas pressure in the subdivertor.

During the first test divertor campaign at Wendelstein 7-X, 13 neutral gas pressure gauges in different positions in the midplane of the plasma vessel and in the subdivertor provided an overview over the neutral gas pressures obtained during divertor operation. Depending on the line integrated electron density and the magnetic field configuration, neutral gas pressures of up to 1.75×10^{-3} mbar were obtained in the high iota section of the subdivertor in the high iota configuration. In the standard, high mirror and low iota configuration, 1.75×10^{-4}–6.00×10^{-4} mbar were reached in the low iota section of the subdivertor, with the maximum values being reached during detached discharges. Consequently, the flux of pumped particles was highest in the high iota section of the subdivertor during discharges in high iota configuration with 1.0×10^{20} $\mathrm{a\,s^{-1}}$ being exhausted. Despite the lower pumping speed in the high iota section, the AEP port accounts for 90% of the exhausted particles in the high iota configuration and still 18% of the exhausted particles in standard configuration due to the neutral gas pressure in the high iota section.

The compression ratio, which is often used to assess divertor performance, does not determine gas exhaust, but is a measure for the neutral gas pressure in the midplane at a given subdivertor neutral gas pressure. As increased neutral gas pressures in the midplane lead to charge exchange processes generating fast neutrals that can damage the plasma facing components, low neutral gas pressures in the midplane are required to avoid damage while high neutral gas pressures in the subdivertor are needed for efficient particle exhaust. Similar neutral gas pressures in the midplane were obtained during discharges in standard and high iota configuration, leading to the compression at the pumping ports being twice as high with values of 50–125 at the AEP port in high iota configuration compared to values of 20–60 at the AEH port in standard configuration. In the high mirror and low iota configuration, compression ratios of 20–40 and 10–50 at the AEH port were obtained.

The different neutral gas pressures in the low and high iota section of the subdivertor and thus the different compression ratios are a consequence of the inhomogeneous pressure distribution in the subdivertor volume, which is separated into a low iota section and a high iota section by a poloidal shield. The pressure ratio between the low iota and the high iota section was experimentally found to be around 0.06 for the high iota configuration and 2–5 for the other configurations, revealing that even with the strike line on the targets in the low iota section of the divertor, surprisingly high neutral gas pressures are still measured at the AEP ports in the high iota section, suggesting a more advantageous divertor geometry in the high iota section concerning particle collection and retention.

For two reference discharges in standard and high iota configuration, the pressure distribution in the subdivertor was calculated using a finite element simulation in ANSYS. The particle fluxes through the large and small pumping gap into the subdivertor were calculated by EMC3-EIRENE and then used as an input for the ANSYS simulation. In the standard configuration, the particle flux through the large pumping gap is 12 times larger than through the small pumping gap. In high iota configuration, the ratio of the particle fluxes through the large and small pumping gap into the subdivertor is 0.4. H_α-measurements of the recycling flux in front of the divertor targets can be used as a proxy of the neutral particle flux through the pumping gaps and served as an experimental estimate for these ratios.

The finite element simulation as well as a steady state estimate of the neutral gas pressure in both subdivertor sections result in accurate predictions of the neutral gas pressure in the low iota section of the subdivertor for standard and high iota configurations. However, the neutral gas pressures in the high iota section of the subdivertor are underestimated in both models compared to the experimental results due to the unknown volume and leakage area of the subdivertor sections that are surrounded by the closure plates.

Data availability statement

The data cannot be made publicly available upon publication because they are not available in a format that is sufficiently accessible or reusable by other researchers. The data that support the findings of this study are available upon reasonable request from the authors.

Acknowledgments

This work has been carried out within the framework of the EUROfusion Consortium, funded by the European Union via the Euratom Research and Training Programme (Grant Agreement No. 101052200—EUROfusion). Views and opinions expressed are however those of the author(s) only and do not necessarily reflect those of the European Union or the European Commission. Neither the European Union nor the European Commission can be held responsible for them.

ORCID iDs

V Haak https://orcid.org/0000-0001-9158-5566
S A Bozhenkov https://orcid.org/0000-0003-4289-3532
A Kharwandikar https://orcid.org/0000-0001-7272-1198
T Kremeyer https://orcid.org/0000-0002-6383-944X
D Naujoks https://orcid.org/0000-0003-4265-6078
V Perseo https://orcid.org/0000-0001-8473-9002
G Schlisio https://orcid.org/0000-0002-5430-0645
U Wenzel https://orcid.org/0000-0002-4107-9291

References

[1] Beidler C *et al* 1990 Physics and engineering design for Wendelstein VII-X *Fusion Technol.* **17** 148–68
[2] Klinger T *et al* (The Wendelstein 7-X Team) 2013 Towards assembly completion and preparation of experimental campaigns of Wendelstein 7-X in the perspective of a path to a stellarator fusion power plant *Fusion Eng. Des.* **88** 461–5
[3] Bosch H-S *et al* 2017 Final integration, commissioning and start of the Wendelstein 7-X stellarator operation *Nucl. Fusion* **57** 116015
[4] Klinger T *et al* 2017 Performance and properties of the first plasmas of Wendelstein 7-X *Plasma Phys. Control. Fusion* **59** 014018
[5] Pedersen T S *et al* 2017 Key results from the first plasma operation phase and outlook for future performance in Wendelstein 7-X *Phys. Plasmas* **24** 055503
[6] Wolf R C *et al* 2017 Major results from the first plasma campaign of the Wendelstein 7-X stellarator *Nucl. Fusion* **57** 102020
[7] Fujiwara M *et al* 2001 Overview of LHD experiments *Nucl. Fusion* **41** 1355
[8] Artsimovich L A 1972 Tokamak devices *Nucl. Fusion* **12** 215
[9] Feng Y, Sardei F, Grigull P, McCormick K, Kisslinger J and Reiter D 2006 Physics of island divertors as highlighted by example of W7-AS *Nucl. Fusion* **46** 807–19
[10] König R *et al* 2002 The divertor program in stellarators *Plasma Phys. Control. Fusion* **44** 2365
[11] Renner H, Boscary J, Greuner H, Grote H, Hoffmann F, Kisslinger J, Strumberger E and Mendelevitch B 2002 Divertor concept for the W7-X stellarator and mode of operation *Plasma Phys. Control. Fusion* **44** 1005
[12] Grigull P *et al* 2001 First island divertor experiments on the W7-AS stellarator *Plasma Phys. Control. Fusion* **43** A175
[13] Hirsch M *et al* 2008 Major results from the stellarator Wendelstein 7-AS *Plasma Phys. Control. Fusion* **50** 053001
[14] Pedersen T S *et al* 2019 First results from divertor operation in Wendelstein 7-X *Plasma Phys. Control. Fusion* **61** 015035
[15] Gao Y, Jakubowski M W, Drewelow P, Pisano F, Puig Sitjes A, Niemann H, Ali A and Cannas B 2019 Methods for quantitative study of divertor heat loads on W7-X *Nucl. Fusion* **59** 066007
[16] Kremeyer T 2019 Particle fueling and exhaust in the Wendelstein 7-X island divertor *PhD Thesis* The University of Wisconsin-Madison
[17] Wenzel U, Pedersen T S, Marquardt M and Singer M 2018 An ionization pressure gauge with LaB_6 emitter for long-term operation in strong magnetic fields *Rev. Sci. Instrum.* **89** 033503
[18] Schlisio G *et al* 2021 The evolution of the bound particle reservoir in Wendelstein 7-X and its influence on plasma control *Nucl. Fusion* **61** 036031
[19] Schmitz O *et al* (The W7-X Team) 2021 Stable heat and particle flux detachment with efficient particle exhaust in the island divertor of Wendelstein 7-X *Nucl. Fusion* **61** 016026
[20] Boscary J, Ehrke G, Greuner H, Junghanns P, Li C, Mendelevitch B, Springer J and Stadler R 2021 Completion of the production of the W7-X divertor target modules *Fusion Eng. Des.* **166** 112293
[21] Boscary J, Friedrich T, Greuner H, Schulmeyer W, Stadler R, Mendelevitch B, Junghanns P and Ehrke G 2017 Summary of the production of the divertor target elements of Wendelstein 7-X *Fusion Eng. Des.* **124** 348–51
[22] Boscary J, Peacock A, Stadler R, Mendelevitch B, Tittes H, Tretter J, Smirnow M and Li C 2013 Actively water-cooled plasma facing components of the Wendelstein 7-X stellarator *Fusion Sci. Technol.* **64** 263–8
[23] Mendelevitch B, Vorköper A, Boscary J, Li C, Dekorsy N, Peacock A, Sellmeier O, Stadler R and Tittes H 2013 Lessons learned from the design and fabrication of the baffles and heat shields of Wendelstein 7-X *Fusion Eng. Des.* **88** 1660–3
[24] Boscary J, Schauer F, Ghidersa B-E, Krüßmann R, Lux M, Czerwinski M, Wang Z, Li C, Mendelevitch B and Ehrke G 2022 Thermal loading test of a Wendelstein 7-X pumping gap panel *Fusion Eng. Des.* **175** 112986
[25] Wenzel U *et al* (The W7-X Team) 2022 Gas exhaust in the Wendelstein 7-X stellarator during the first divertor operation *Nucl. Fusion* **57** 096016
[26] Ehrke G, Mendelevitch B, Boscary J, Li C, Sellmeier O, Stadler R, McNeely P and Schauer F 2019 Design and manufacturing of the Wendelstein 7-X cryo-vacuum pump *Fusion Eng. Des.* **146** 2757–60
[27] Streibl B *et al* 2009 (Max-Planck-Institut für Plasmaohysik) Ringbuch kryopumpe *IPP Internal Report* 1-ACF-R0002.0
[28] Feng Y *et al* 2022 Review of magnetic islands from the divertor perspective and a simplified heat transport model for the island divertor *Plasma Phys. Control. Fusion* **64** 125012
[29] Haas G and Bosch H S 1998 In vessel pressure measurement in nuclear fusion experiments with ASDEX gauges *Vacuum* **51** 39–46
[30] Wenzel U, Schlisio G, Mulsow M, Pedersen T S, Singer M, Marquardt M, Pilopp D and Rüter N 2019 Performance of new crystal cathode pressure gauges for long-pulse operation in the Wendelstein 7-X stellarator *Rev. Sci. Instrum.* **90** 123507

[31] Endler M *et al* 2021 Wendelstein 7-X on the path to long-pulse high-performance operation *Fusion Eng. Des.* **167** 112381
[32] Erckmann V *et al* 1999 ECRH and ECCD with high power gyrotrons at the stellarators W7-AS and W7-X *IEEE Trans. Plasma Sci.* **27** 538–46
[33] Erckmann V *et al* 2007 Electron cyclotron heating for W7-X: physics and technology *Fusion Sci. Technol.* **52** 291–312
[34] Marsen S, Corre Y, Laqua H P, Moncada V, Moseev D, Niemann H, Preynas M and Stange T 2017 First results from protective ECRH diagnostics for Wendelstein 7-X *Nucl. Fusion* **57** 086014
[35] Lazerson S A *et al* 2019 Tuning of the rotational transform in Wendelstein 7-X *Nucl. Fusion* **59** 126004
[36] Gao Y *et al* 2019 Effects of toroidal plasma current on divertor power depositions on Wendelstein 7-X *Nucl. Fusion* **59** 106015
[37] Jakubowski M *et al* (The W7-X Team) 2021 Overview of the results from divertor experiments with attached and detached plasmas at Wendelstein 7-X and their implications for steady-state operation *Nucl. Fusion* **61** 106003
[38] Feng Y *et al* 2021 Understanding detachment of the W7-X island divertor *Nucl. Fusion* **61** 086012
[39] Niemczewski A, LaBombard B, Lipschultz B and McCracken G 1994 Neutral gas compression in the Alcator C-Mod divertor, experimental observations *Technical Report* (Massachusetts Institute of Technology)
[40] Bosch H-S, Ullrich W, Bard A, Coster D, Haas G, Kallenbach A, Neuhauser J and Schneider R (ASDEX Upgrade Team) 1999 Noble gas exhaust with a strongly baffled divertor in ASDEX-Upgrade *J. Nucl. Mater.* **266** 462–6
[41] Morisaki T *et al* 2013 Initial experiments towards edge plasma control with a closed helical divertor in lhd *Nucl. Fusion* **53** 063014
[42] Feng Y, Sardei F, Kisslinger J and Grigull P 1997 A 3D Monte Carlo code for plasma transport in island divertors *J. Nucl. Mater.* **241–243** 930–4
[43] Feng Y, Sardei F and Kisslinger J 1999 3D fluid modelling of the edge plasma by means of a Monte Carlo technique *J. Nucl. Mater.* **266** 812–8
[44] Feng Y *et al* 2014 Recent improvements in the EMC3-Eirene code *Contrib. Plasma Phys.* **54** 426–31
[45] Winters V *et al* 2021 EMC3-EIRENE simulation of first wall recycling fluxes in W7-X with relation to H-alpha measurements *Plasma Phys. Control. Fusion* **63** 045016
[46] Kremeyer T *et al* 2022 Analysis of hydrogen fueling, recycling and confinement at Wendelstein 7-X via a single-reservoir particle balance *Nucl. Fusion* **62** 036023
[47] Wutz M 2004 *Wutz Handbuch Vakuumtechnik* ed K Jousten (Berlin: Springer)
[48] Kallenbach A *et al* 1995 H mode discharges with feedback controlled radiative boundary in the ASDEX Upgrade tokamak *Nucl. Fusion* **35** 1231
[49] Pedersen T S *et al* 2022 Experimental confirmation of efficient island divertor operation and successful neoclassical transport optimization in Wendelstein 7-X *Nucl. Fusion* **62** 042022